HAL
open science

# Anisotropy of electrical conductivity of the Excavation Damaged Zone in the Mont Terri Underground Rock Laboratory

Florence Nicollin, Dominique Gibert, N. Lesparre, Christophe Nussbaum

## To cite this version:

Florence Nicollin, Dominique Gibert, N. Lesparre, Christophe Nussbaum. Anisotropy of electrical conductivity of the Excavation Damaged Zone in the Mont Terri Underground Rock Laboratory. Geophysical Journal International, 2010, 181 (1), pp.303-320. 10.1111/j.1365-246X.2010.04517.x . insu-00600288

**HAL Id: insu-00600288**

**https://insu.hal.science/insu-00600288v1**

Submitted on 6 Jul 2017

**HAL** is a multi-disciplinary open access archive for the deposit and dissemination of scientific research documents, whether they are published or not. The documents may come from teaching and research institutions in France or abroad, or from public or private research centers.

L'archive ouverte pluridisciplinaire **HAL**, est destinée au dépôt et à la diffusion de documents scientifiques de niveau recherche, publiés ou non, émanant des établissements d'enseignement et de recherche français ou étrangers, des laboratoires publics ou privés.

*Geophys. J. Int.* (2010) **181,** 303–320 doi: 10.1111/j.1365-246X.2010.04517.x

# Anisotropy of electrical conductivity of the excavation damaged zone in the Mont Terri Underground Rock Laboratory

Florence Nicollin,[1,4] Dominique Gibert,[2,4] Nolwenn Lesparre[2,4] and Christophe Nussbaum[3,*]

[1] *Géosciences Rennes (CNRS UMR* 6118*), Université Rennes* 1, *Bât.* 15 *Campus de Beaulieu,* 35042 *Rennes cedex, France.*
*E-mail: florence.nicollin@univ-rennes 1.fr*
[2] *Institut de Physique du Globe de Paris (CNRS UMR* 7154*), Université Paris Cité,* 4 *place Jussieu,* 75252 *Paris cedex, France*
[3] *Geotechnisches Institut AG, Gartenstrasse* 13, 3007 *Bern, Switzerland*
[4] *GNR FORPRO II (CNRS-ANDRA)*

Accepted 2010 January 8. Received 2010 January 8; in original form 2009 July 8

## SUMMARY

Electrical resistivity measurements were performed to characterize the anisotropy of electrical resistivity of the excavation damaged zone (EDZ) at the end-face of a gallery in the Opalinus clay of the Mont Terri Underground Rock Laboratory (URL). The data were acquired with a combination of square arrays in 18 zones on the gallery's face and in two series of four boreholes perpendicular to the face. Each data set is independently inverted using simulated annealing to recover the resistivity tensor. Both the stability and the non-uniqueness of the inverse problem are discussed with synthetic examples. The inversion of the data shows that the face is split in two domains separated by a tectonic fracture, with different resistivity values but with a common orientation. The direction of the maximum resistivity is found perpendicular to the bedding plane, and the direction of minimum resistivity is contained in the face's plane. These results show that the geo-electrical structure of the EDZ is controlled by a combination of effects due to tectonics, stratigraphy, and recent fracturing produced by the excavation of the gallery.

**Key words:** Inverse theory; Electrical properties.



## 1 INTRODUCTION

### 1.1 The Mont Terri Underground Rock Laboratory

Among the different rock formations aimed at being valuable host rocks for radioactive waste disposal, argillaceous formations are particularly studied for their remarkable confinement and self-sealing properties (Meier *et al.* 2000). The Mont Terri project (http://www.mont-terri.ch) started in 1995 with the realization of the Underground Rock Laboratory (URL) in a Mesozoic shale formation constituted by the Opalinus clay. The Mont Terri project is a scientific and multidisciplinary and technological platform for geological disposal in argillaceous formations (Thury & Bossart 1999; Bossart & Thury 2008) among which the study of the so-called excavation damaged zone (EDZ) is of a particular importance. The EDZ is produced by the stress changes resulting from the excavation of a gallery and it constitutes a diffuse layer of fractured rock with a variable thickness controlled by the regional stress regime, local tectonics, stratigraphic conditions and the shape of the gallery (Bossart *et al.* 2002). Both the geomechanical and the transport properties of the EDZ are important for galleries aimed at receiving high-level radioactive waste and spent fuel, and several studies have been conducted at the EDZ (Blümling *et al.* 2007; Bossart *et al.* 2002, 2004; Hunsche *et al.* 2004; Martin *et al.* 2004). For further information concerning the EDZ studies the reader is referred to the report by McEwen (2002), and to the extensive review by Bossart & Thury (2008).

Geophysical non-invasive techniques are of a particular interest to assess for the integrity of actual repository galleries where no destructive methods could be used for obvious safety conditions. The seismic methods are particularly efficient to locally investigate the EDZ and to obtain both geometrical and geomechanical data (Schuster *et al.* 2001; Nicollin *et al.* 2008). While the seismic technique is particularly efficient when used in boreholes, non-destructive seismic reflection and surface wave methods also provide useful information. Recent studies (e.g. Kruschwitz & Yaramanci 2004; Gibert *et al.* 2006) demonstrate that electrical tomography constitutes an interesting method to probe the EDZ and monitor its evolution. Electrical resistance tomography has the advantage of being a cheap method allowing to easily install extended

*Now at: Swisstopo, Federal Office for Topography, Seftingenstrasse 264, CH-Wabern, Switzerland.

© 2010 The Authors
Journal compilation © 2010 RAS

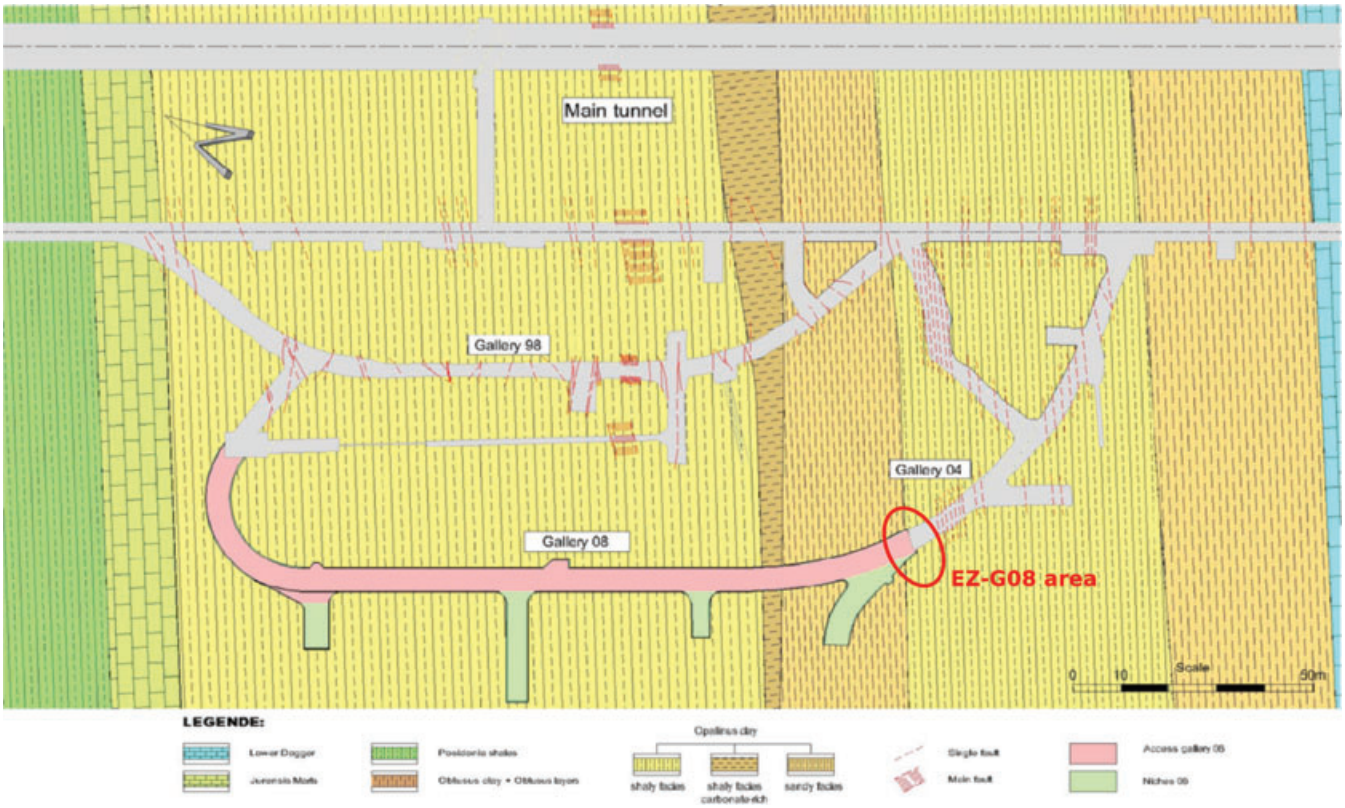


**Figure 1.** Geological map and global view of the Mont Terri URL as completed in 2008. The Gallery Ga04 is located at the southern side of the URL and the new gallery Ga08 appears in pink. The experimental EZ-G08 area is located at the junction between the two galleries.

permanent electrode arrays in order to investigate large volumes of the EDZ. These permanent arrays can be used to perform repetitive surveys to study the long-term evolution of the rock mass.

In this paper, we present a detailed study of the electrical anisotropy properties of the EDZ located behind the end face of the gallery Ga04 excavated in year 2004. This study was done in the framework of a large multidisciplinary project aimed at monitoring the evolution of a rock mass segment during the excavation of a new gallery.

### 1.2 The EZ-G08 experiment

The EZ-G experiments aim at following the time and space evolution of the EDZ during the excavation of a gallery of large (5 m) diameter. The EZ-G04 experiment began in 2004 July with arrays of electrodes installed to follow the evolution of the EDZ during the restart of the excavation of the gallery Ga04. The electrical tomography survey performed during the excavation allowed to observe the evolution of the EDZ at time constants ranging from one week to several years (Gibert *et al.* 2006). The EZ-G08 experiment, launched in September 2007, was designed to study the evolution of the EDZ at timescales ranging from hours to months and was installed at the end face of the gallery Ga04 to observe the arrival of the excavation face of the new gallery Ga08 (Fig. 1).

The gallery Ga04 has a total length of 80 m and is located at the southern end of the URL. It was entirely excavated in the shaly facies of the Opalinus clay with its entrance section oriented in a WE direction and its axis making an angle of 20° northward with respect to the bedding strike. The end part of this gallery is oriented in a NW–SE direction and its axis makes an angle of 50° northward with respect to the bedding strike. The gallery Ga08 has a total length of 167 m and was first (and mostly) excavated in the shaly facies, followed by a short portion crossing the carbonate-rich sandy facies and a final part in the sandy facies. The segment of rock studied in the EZ-G08 experiment has a length of 8 m and is located in the 159– 167 m interval of the gallery Ga08 geodetic reference frame. The 159–165 m part of the EZ-G08 segment is in the sandy facies and the 165–167 m part is in the shaly facies. So, when seen from the end face of the gallery Ga04, the studied volume of rock consists of 2 m of shaly clay followed by 6 m of sandy clay. Let us remark that the part of the EZ-G08 segment limited by the end face of the gallery Ga04 is damaged since the end of 2004 when the gallery was totally excavated while the opposite part of the segment was damaged only since the end of 2008 June when the excavation face of the gallery Ga08 arrived at its proximity.

In this paper, we focus on geo-electrical measurements providing information about the anisotropy of the electrical conductivity in the part of the rock mass segment damaged since 2004, hereafter called the EDZ-04 of the EZ-G section.

## 2 FIELD EXPERIMENTS

### 2.1 Layout of electrode arrays and measurements

The data analysed in the present study have been acquired with an array of more than 700 electrodes installed on the Ga04 face (Fig. 2). The electrodes are stainless steel rods of 8 mm in diameter and 8 cm in length. They were placed in the clay by soft hammering to enter in holes of 7 mm in diameter and a few centimetres in length drilled in the clay. We checked that this procedure ensured a good electrical

**Figure 2.** General view of the geophysical monitoring system installed on the Ga04 side of the EZ-G section. A tectonic fracture (SW dipping fault N 120–20°) well visible on the face is marked by a black dashed line. The white mesh has a mean side of 30 cm and represents the mesh formed by horizontal and vertical lines of the array of 700 electrodes installed to perform a detailed electrical tomography of the EDZ-04. The distance between the electrodes along the lines is 15 cm.

contact and, indeed, only a few electrodes needed to be repaired during the experiment. The electrode array covers the rough face according to a square mesh with a mean side of 30 cm. On each line of the mesh, the electrodes are equally spaced every 15 cm. A topographic survey was done to obtain the precise 3-D-position of each electrode of the array.

The electrode array was first used to perform a global resistivity survey of the face with Wenner resistivity measurements with aligned and equally spaced electrodes placed according to the geometrical sequence $\{A, M, N, B\}$ . $A$ and $B$ represent the electrodes used to inject the electrical current and $M$ and $N$ are the electrodes where the electrical potential $\Delta V(A, B, M, N)$ is measured (e.g. Apparao *et al.* 1992). Reciprocal measurements corresponding to the sequence $\{M, A, B, N\}$ have also been made in order to check the reliability of the apparatus. Wenner resistivity profiles were performed both along the horizontal and the vertical lines of the face shown in Fig. 3(a) with an along-line sampling of 15 cm and a distance of 30 cm between profiles. Each of the 10 lowest horizontal lines counts 32 electrodes, and the 3 highest lines count 30 or 31 electrodes. In the vertical direction, the length of the lines is more variable and varies from 2.70 m (i.e. 19 electrodes) for the shortest line at the NE side to 4.65 m (i.e. 32 electrodes) for the nine longest lines. Lines counting 32 or 30 electrodes allowed to perform 155 or 145 Wenner measurements, respectively, while only 40 measurements were possible for lines with 19 electrodes.

Other measurements, best adapted to the study of electrical resistivity anisotropy, were done with the so-called square array configuration where the electrodes are located at the corners of squares with different sizes and orientations (Habberjam 1972). We used the so-called $\alpha$ and $\beta$ configurations where the $A$ and $B$ current electrodes

© 2010 The Authors, *GJI*, **181,** 303–320
Journal compilation © 2010 RAS

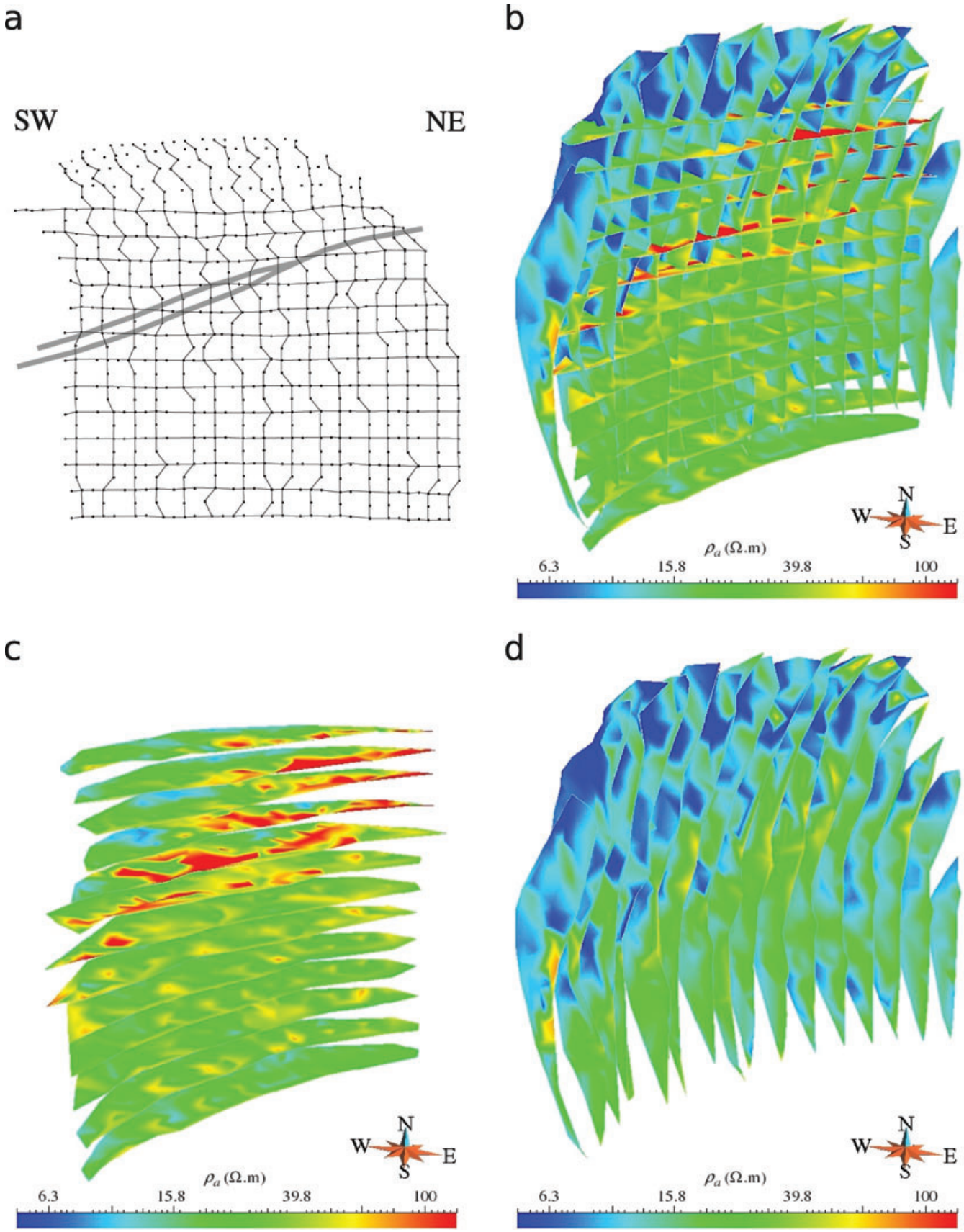


**Figure 3.** Global electrical tomography of the Ga04 face with Wenner profiles performed along (a) 13 horizontal lines and 16 vertical lines of up to 32 electrodes. The trace of the main fracture visible on the face is marked by a grey line. (b) Pseudo-sections of apparent resistivity $\rho_a$ of all the Wenner profiles. (c) Pseudo-sections of the Wenner profiles performed along the horizontal lines. (d) Pseudo-sections of the Wenner profiles performed along the vertical lines.

© 2010 The Authors, *GJI*, **181,** 303–320
Journal compilation © 2010 RAS

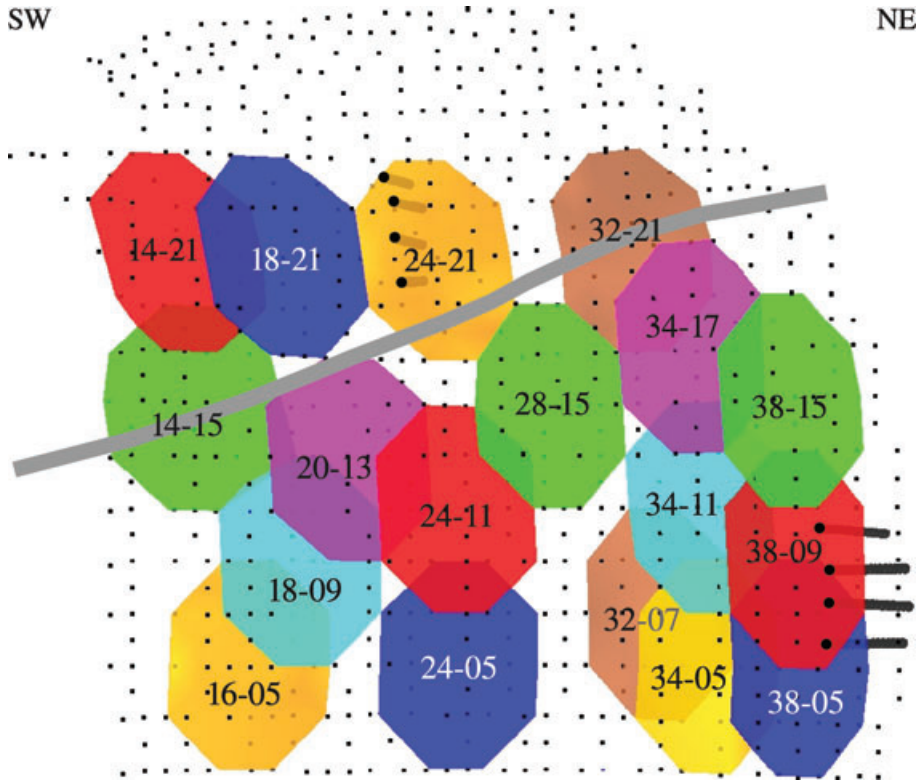


**Figure 4.** Location of 18 areas of 32 electrodes on the face and two series of four boreholes equipped with lines of 16 electrodes, used for anisotropy measurements with the square array configuration. Five areas (called 14-15, 14-21, 18-21, 24-21 and 32-31) are located in the domain above the fracture, while the other 13 areas are located in the lower compartment. One group of boreholes is located in the 24-21 zone of the upper domain, and the other group is located in the 38-09 zone of the lower domain.

define one side of the square, and the $M$ and $N$ potential electrodes define the opposite side. Thus, with one square, it is possible to measure the electrical resistivity in two perpendicular directions given by the orientation of the $AB$ side. Most square measurements were done with 18 groups of 32 electrodes located on the gallery's face, each group occupying an area of about 1.2 m high by 0.9 m wide (Fig. 4). Five areas were located in the domain located above the main fracture and 13 areas were located in the domain below. A group of 32 electrodes as shown in Fig. 5(a) allows to define 59 squares arrangements, producing 118 measurements of the electrical resistivity in 12 directions and for seven depths related to the size of the square (Fig. 5b). In addition, two groups of four small-size subparallel boreholes were used to make measurements in a plane perpendicular to the face (Fig. 4). These boreholes were also 3-D-located by topographic survey: they are subhorizontal, spaced about 20 cm, and have a diameter of 42 mm and a length of 1 m. One group of the boreholes was located in the compartment above the main fracture, and the other group was located in the lower domain. Each borehole was equipped with a line of 16 electrodes equally spaced of 5 cm. Thus, in the two groups of boreholes, 64 electrodes define 56 quadrilaterals close to the square shape (Fig. 5c), producing 112 measurements of the electrical resistivity in 8 directions and over four depths (Fig. 5d).

The equipment used for these experiments is an ABEM SAS4000 resistivity metre coupled with an ES464 multi-electrode switcher that manages up to 64 electrodes. The switcher may be configured to arbitrarily select the $\{A, B, M, N\}$ electrodes to perform a given measurement. The measurement procedure begins by injecting a low-frequency square-shaped alternating current in order to suppress polarization of the electrodes. The electrical potential $\Delta V$ is measured in phase with the current injection to enhance the signal-to-noise ratio.

### 2.2 Presentation of the data

The Wenner measurements performed along the horizontal and vertical lines of the array are shown in Fig. 3 as pseudo-sections of the apparent resistivity. For the Wenner geometry, pseudo-sections are simply obtained by assigning the apparent resistivity value, $\rho_a$, to a point $P$ located at the middle of the quadrupole and at a depth equal to the distance between electrodes (Edwards 1977; Barker 1989). The apparent resistivity is computed by applying a geometrical factor $K$ to the measured electrical resistance $\Delta V(A, B, M, N)/I$, where $I$ is the electrical current actually injected. $K$ is such that, for a medium with a constant isotropic resistivity $\rho$, the apparent resistivity $\rho_a$ equals $\rho$. This implies that the geometrical factor must properly account for the exact 3-D-position of each electrode. Fig. 3(b) presents the assemblage of all the pseudo-sections obtained with the Wenner profiles, while Figs 3(c) and (d) present the pseudo-sections of the horizontal lines and of the vertical lines, respectively. These figures clearly show that the apparent resistivity depends on the direction in which it is measured, highlighting an anisotropy of electrical conductivity. The apparent resistivity measured along horizontal profiles is higher than the one measured along vertical profiles. Moreover, especially on horizontal profiles, the main fracture visible on the Ga04 face appears as a high-resistive zone that separates two domains with different apparent resistivity. On each of the two assemblages, the apparent resistivity measured in the

© 2010 The Authors, *GJI*, **181,** 303–320
Journal compilation © 2010 RAS

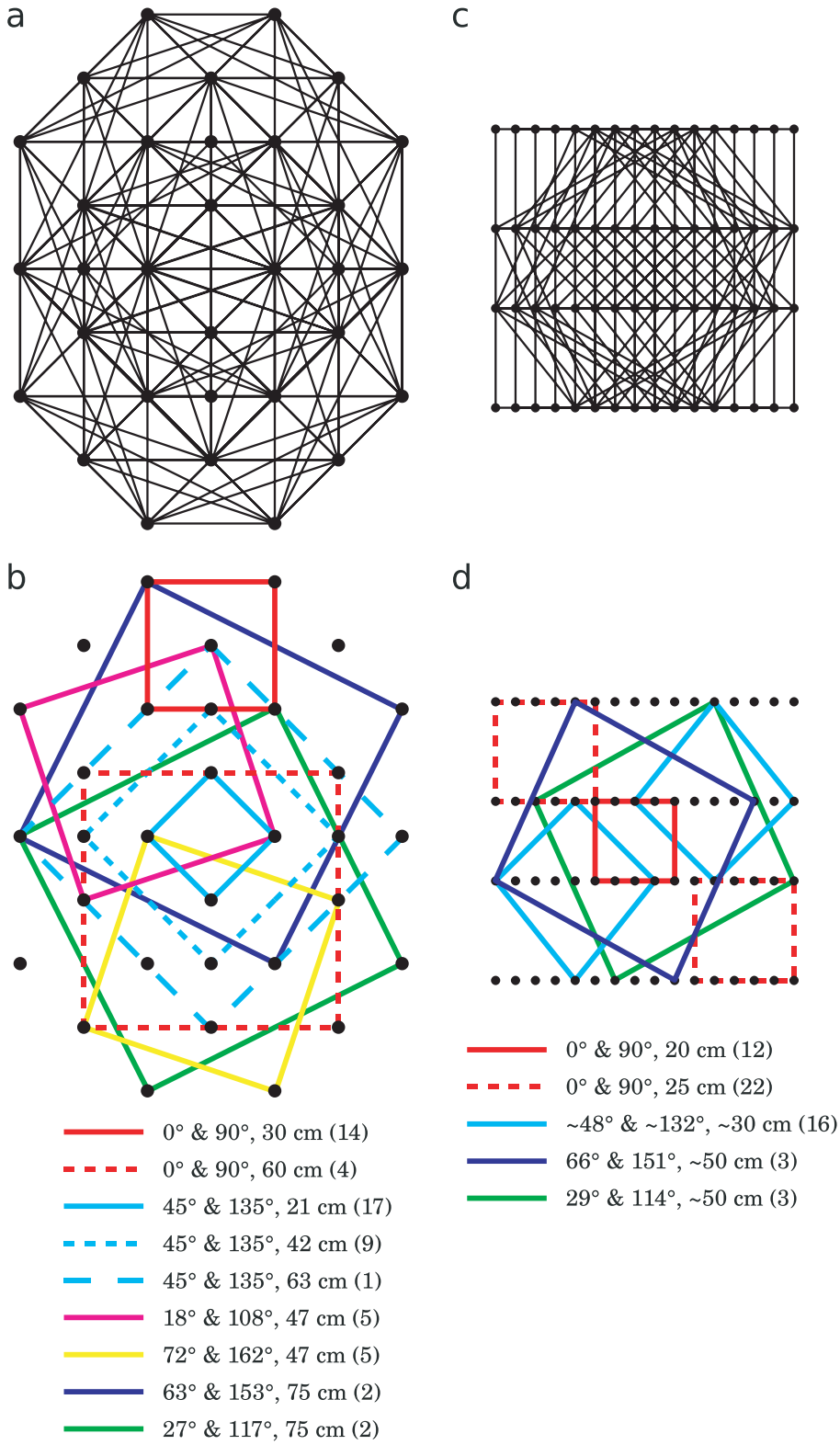


**Figure 5.** Square array for: (a) a set of 32 electrodes on the face [59 squares of various orientations and sizes shown in (b)] and (c) 64 electrodes in the four boreholes of the lower domain [56 squares of various orientations and sizes shown in (d)]. The orientation is given by the angle between one side of the square and the horizontal axis, the number of squares of each kind is given between parenthesis.

upper domain displays lower values than the one measured in the lower domain. The paradox of electrical anisotropy says that, when measured with aligned electrodes, the apparent resistivity appears higher on profiles arranged in a direction of low resistivity than on profiles arranged in a direction of high resistivity (Habberjam 1972).

In anisotropic medium, measurements done with the square array configuration do not contain ambiguity: the apparent resistivity

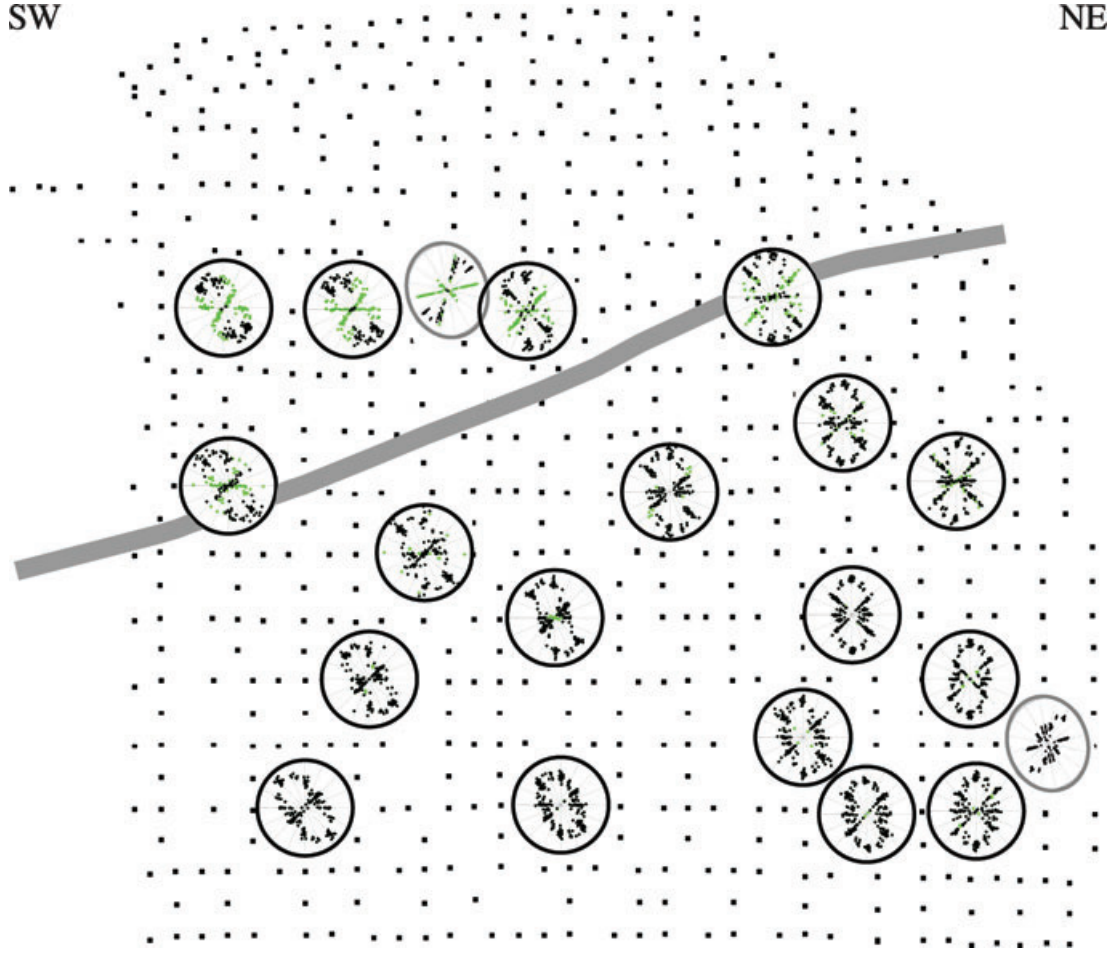


**Figure 6.** Polar diagrams showing the apparent resistivity measured using the square array configuration, in the 18 areas of the face (diagrams with black border) and in the two areas of four boreholes (diagrams with grey border). The diagram radius represents the resistivity between 0 and 316 Ωm with a logarithmic scale, and the angle from the horizontal axis of the diagram corresponds to the dip of the *AB* segment. Black dots represent positive values of apparent resistivity while green dots represent negative values of apparent resistivity.

measured in the direction of the *AB* segment varies in accordance with the true resistivity tensor (e.g. Habberjam 1972; Senos Matias 2002). Fig. 6 displays such measurements performed on the Ga04 face, with apparent resistivity plotted in polar diagrams. All the measurements made in each area are plotted in one diagram, so that the whole experiment is represented by 20 diagrams: five diagrams on the face and one diagram in boreholes for the upper domain above the main fracture, 13 diagrams on the face and one diagram in boreholes for the lower domain. These diagrams clearly show the anisotropy of electrical conductivity: on the face, the highest values of apparent resistivity are measured in a direction close to the vertical, and negative values of apparent resistivity confirm the existence of a strong anisotropy, especially in the upper domain. Moreover, the direction of highest apparent resistivity measured on the face turns from the SW side where it makes an angle of about 40° from the vertical, to the NE side where it is close to the vertical. These data, measured according to the square array configuration, were used to recover the tensor of electrical conductivity, by inversion process.

## 3 INVERSE PROBLEM

In this section, we present the methodology used to derive the anisotropic conductivity from the data presented above. First, we briefly discuss the forward modelling used to obtain synthetic data corresponding to a given conductivity of the medium and for an electrode arrangement similar to the one used in the gallery. Next, we present the inversion strategy adopted in this study, which is based on a Bayesian approach coupled with a non-linear Monte Carlo method. Finally, we discuss some synthetic examples to illustrate the ill-posedness of the inversion.

### 3.1 The forward problem

The forward problem consists in solving the Ohm's law expressed as

$$\mathbf{J} = \underline{\underline{\sigma}} \cdot \mathbf{E}, \tag{1}$$

where **J** and **E** are the electrical current density and the electrical field, respectively. The conductivity tensor is given by,

$$\underline{\underline{\sigma}} = \begin{pmatrix} \sigma_{xx} & \sigma_{xy} & \sigma_{xz} \\ \sigma_{yx} & \sigma_{yy} & \sigma_{yz} \\ \sigma_{zx} & \sigma_{zy} & \sigma_{zz} \end{pmatrix}. \tag{2}$$

with $\sigma_{\alpha\beta} = \sigma_{\beta\alpha}$ to ensure symmetry.

To have a unique solution eq. (1) must be completed with suitable boundary conditions. In this study, the domain occupied by the

© 2010 The Authors, *GJI*, **181,** 303–320
Journal compilation © 2010 RAS

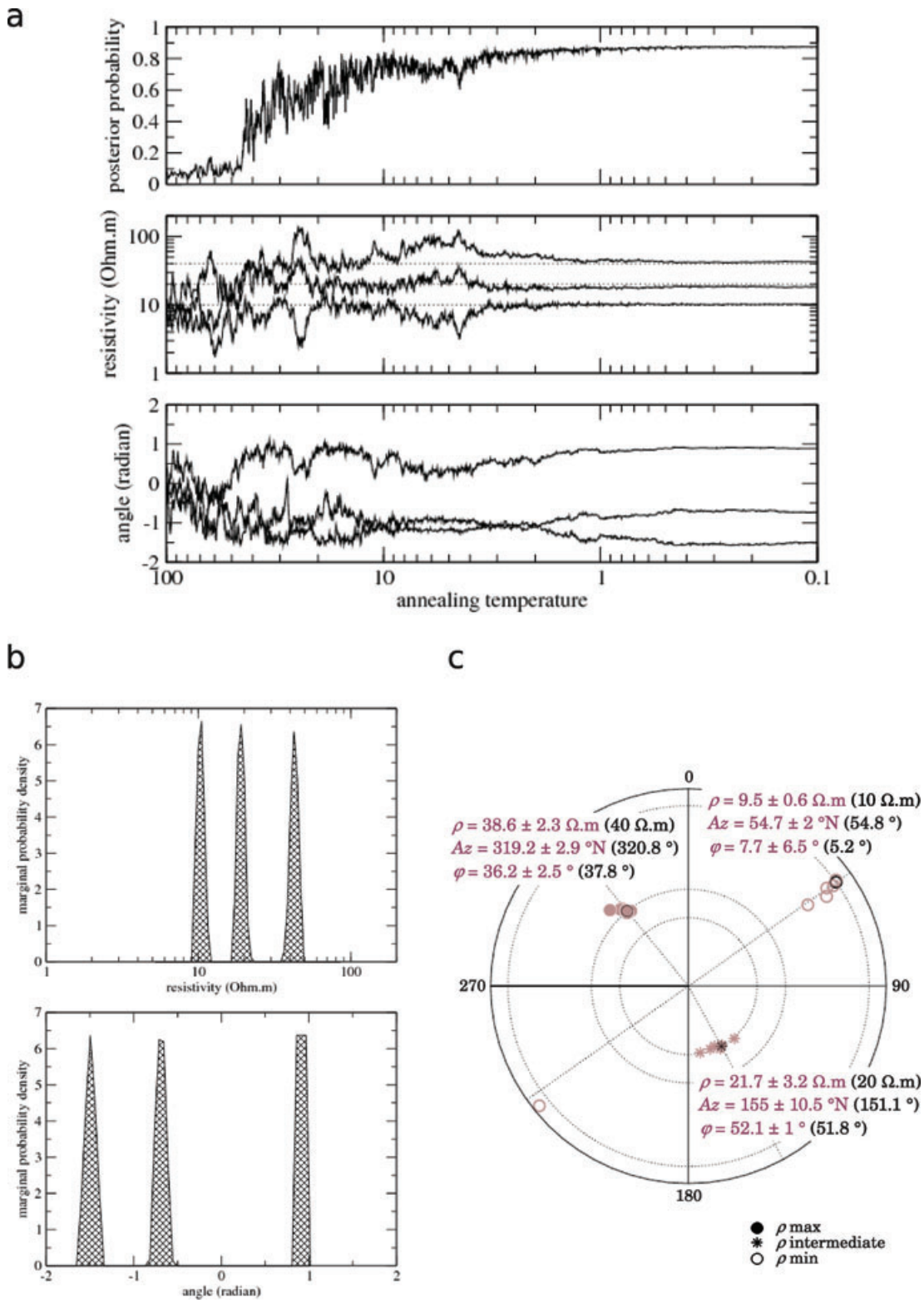


**Figure 7.** Inversion process of synthetic data obtained with electrodes placed in two perpendicular planes (the gallery's face and a set of four boreholes) of an anisotropic medium: (a) likelihood curve of the models forming the Metropolis chain versus annealing temperature, and parameters to be inverted $\{\rho_1, \rho_2, \rho_3, \theta_x, \theta_y, \theta_z\}$ versus annealing temperature, with $\rho = \exp(-\log\sigma)$ (the 3 resistivity values used to compute the synthetic data are plotted with dotted lines); (b) probability distribution of the parameters of the final model and (c) Wulff stereographic projection (angle preserving, lower hemisphere) showing the azimuths and dips corresponding to the parameters $\theta$ of the models obtained at the final stage of six inversion processes (the azimuths and dips used to compute the synthetic data are plotted with black symbols and dotted lines).

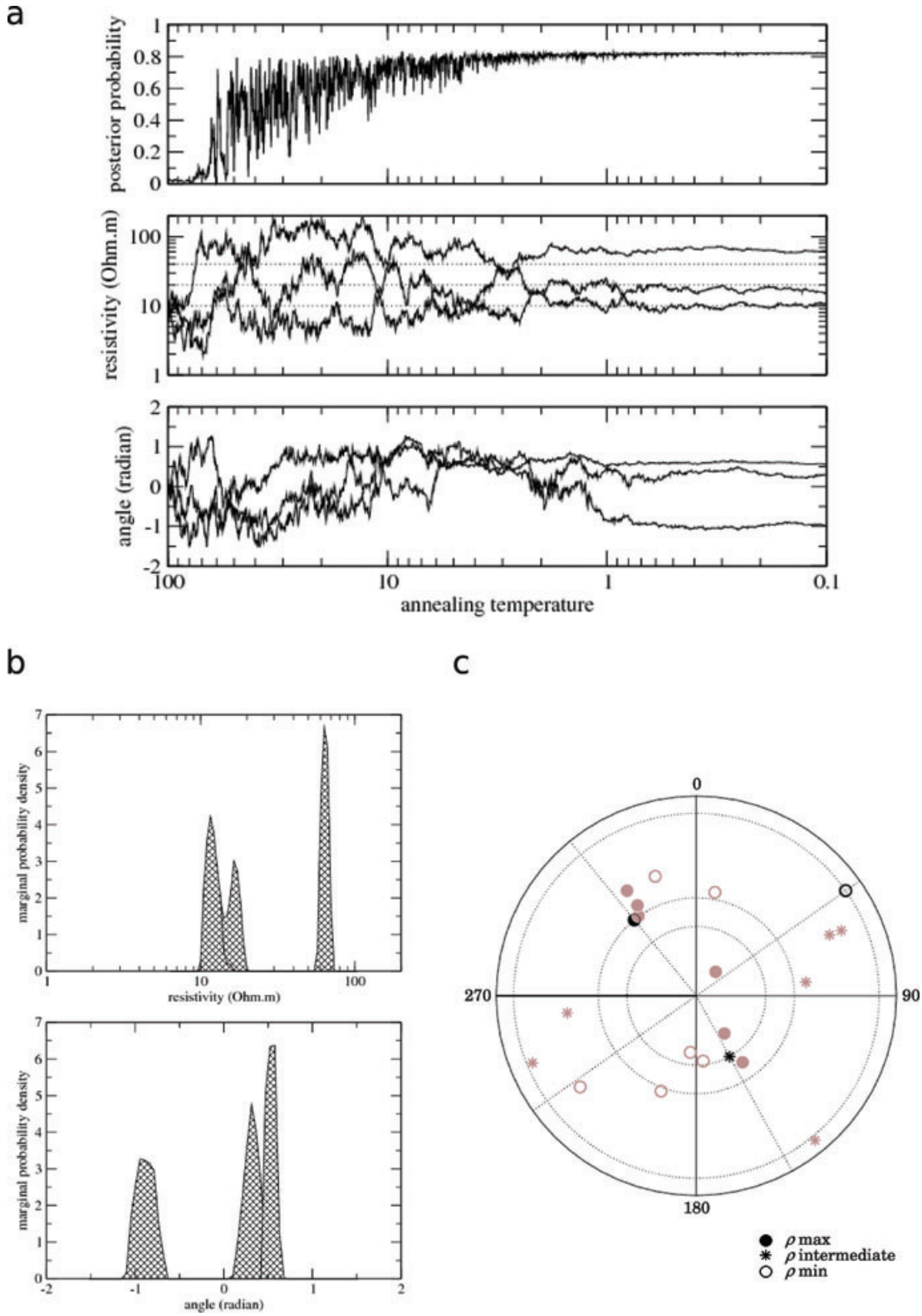


**Figure 8.** Inversion process of synthetic data obtained with electrodes placed in 1 plane (the gallery's face) of an anisotropic medium: (a) likelihood curve of the models forming the Metropolis chain versus annealing temperature, and parameters to be inverted $\{\rho_1, \rho_2, \rho_3, \theta_x, \theta_y, \theta_z\}$ versus annealing temperature, with $\rho = \exp(-\log\sigma)$ (the 3 resistivity values used to compute the synthetic data are plotted with dotted lines); (b) probability distribution of the parameters of the final model and (c) Wulff stereographic projection (angle preserving, lower hemisphere) showing the azimuths and dips corresponding to the parameters $\theta$ of the models obtained at the final stage of six inversion processes (the azimuths and dips used to compute the synthetic data are plotted with black symbols and dotted lines).

© 2010 The Authors, *GJI*, **181,** 303–320
Journal compilation © 2010 RAS

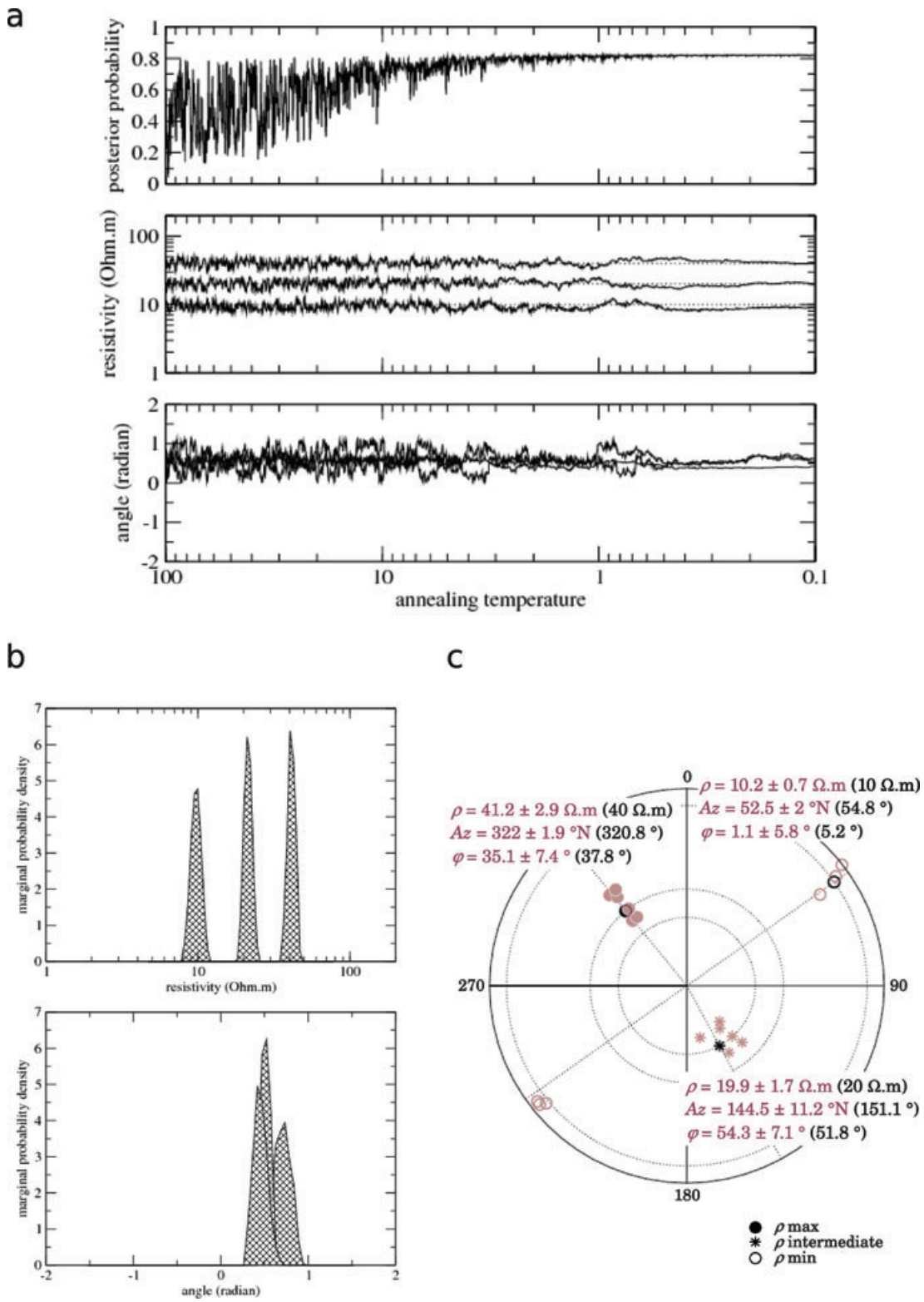


**Figure 9.** Constrained-inversion process of synthetic data obtained with electrodes placed in one plane (the gallery's face) of an anisotropic medium: (a) likelihood curve of the models forming the Metropolis chain versus annealing temperature, and parameters to be inverted $\{\rho_1, \rho_2, \rho_3, \theta_x, \theta_y, \theta_z\}$ versus annealing temperature, with $\rho = \exp(-\log\sigma)$ (the three resistivity values used to compute the synthetic data are plotted with dotted lines); (b) probability distribution of the parameters of the final model; (c) Wulff stereographic projection (angle preserving, lower hemisphere) showing the azimuths and dips corresponding to the parameters $\theta$ of the models obtained at the final stage of six inversion processes (the azimuths and dips used to compute the synthetic data are plotted with black symbols and dotted lines).

© 2010 The Authors, *GJI*, **181,** 303–320
Journal compilation © 2010 RAS

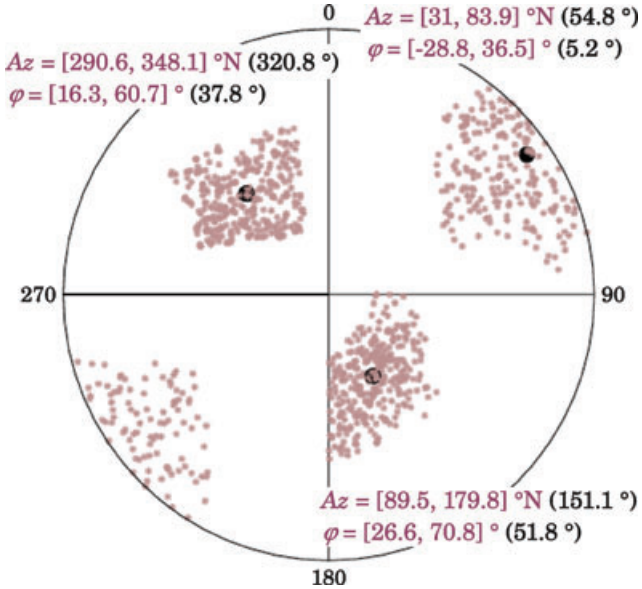


**Figure 10.** Wulff stereographic projection (angle preserving, lower hemisphere) showing the statistical distribution of the azimuths and dips obtained with 300 random variations in the range $-\frac{\pi}{9}, \frac{\pi}{9}]$ of the parameters $\{\theta_x, \theta_y, \theta_z\}$. The azimuths and dips corresponding to the undisturbed parameters are plotted with black-filled circles.

electrodes for each series of measurements is so reduced that the gallery's face can be locally considered plane. We then shall adopt a half-space geometry with the $z = 0$ plane taken as an insulating boundary representing the gallery's face and the conducting domain (i.e. the rock) corresponding to $z \geq 0$. Furthermore, because of the small amount of data available we shall assume a constant anisotropic conductivity. With these simplifying assumptions, the problem is analytically tractable and, for the full-space case, the electrical potential at an electrode $\mathbf{r}_e$ produced by a unit current source point $\mathbf{r}_s$ reads (Das & Li 1996),

$$V_f(\mathbf{r}_e|\mathbf{r}_s) = \frac{1}{4\pi}\sqrt{\frac{\det \underline{\underline{\rho}}}{(\mathbf{r}_e - \mathbf{r}_s)^t \underline{\underline{\rho}}(\mathbf{r}_e - \mathbf{r}_s)}}, \tag{3}$$

where $\underline{\underline{\rho}}$ is the electrical resistivity tensor with components $\rho_{\alpha\beta} = \sigma^{-1}_{\alpha\beta}$. In practice, the resistivity tensor is often given in terms of both its principal values, $(\rho_1, \rho_2, \rho_3)$, expressed in Ω. m and their associated principal directions, $(Az_1, \varphi_1; Az_2, \varphi_2; Az_3, \varphi_3)$, where $Az$ and $\varphi$ are the azimuth and the dip, respectively. Thus, these directions may be plotted in stereographic projection diagram. In this paper, we adopted the Wulff projection of the lower hemisphere, where the angle are preserved, the azimuth being read on the perimeter and the dip on the radius from the edge (e.g. a line dipping a few degrees towards the SE is represented by a point near the edge of the right lower quadrant).

The boundary condition corresponding to the half-space geometry is imposed by using the image method, and the Green's potential takes the form (Das & Li 1996),

$$V_h(\mathbf{r}_e|\mathbf{r}_s) = V_f(\mathbf{r}_e|\mathbf{r}_s) + V_f(\mathbf{r}_e|\mathbf{r}_s^i), \tag{4}$$

where $\mathbf{r}_s^i$ is the location of the source image. Because of the electrical field distortion produced by anisotropy, the location of the image with respect to both the plane boundary and the primary source is not simple and may be found in Li & Uren (1997).

**Table 1.** Results of inversion of each set of data of the face with the data of the appropriate group of boreholes.

| Zone | $\rho_1$ (Ωm) | $Az_1$ (° N) | $\varphi_1$ (°) | $\rho_2$ (Ωm) | $Az_2$ (°N) | $\varphi_2$ (°) | $\rho_3$ (Ωm) | $Az_3$ (°N) | $\varphi_3$ (°) |
|---|---|---|---|---|---|---|---|---|---|
| 14-15 | 8.7 | 234.3 | −1.6 | 19.8 | 142.8 | 46.4 | 156.2 | 319.8 | 44.9 |
| 14-21 | 4.9 | 236.0 | −0.7 | 30.2 | 142.6 | 49.7 | 211.7 | 321.3 | 41.8 |
| 18-21 | 3.1 | 243.1 | −3.0 | 33.4 | 152.1 | 49.9 | 267.0 | 326.4 | 41.2 |
| 24-21 | 8.0 | 234.2 | 4.8 | 16.3 | 135.3 | 46.4 | 174.4 | 323.1 | 44.1 |
| 32-21 | 7.8 | 239.6 | 2.4 | 40.4 | 144.9 | 52.2 | 199.5 | 329.1 | 37.9 |
| Mean | 6.5 | 237.4 | 0.4 | 28.0 | 143.5 | 48.9 | 201.8 | 323.9 | 42.0 |
| *SD* | 2.4 | 3.8 | 3.2 | 9.9 | 6.0 | 2.5 | 42.4 | 3.8 | 2.8 |
| 16-05 | 8.0 | 190.3 | 36.8 | 26.6 | 72.8 | 31.9 | 51.9 | 314.6 | 37.1 |
| 18-09 | 7.4 | 203.3 | 29.4 | 23.9 | 89.3 | 35.8 | 59.0 | 321.7 | 40.2 |
| 20-13 | 7.2 | 211.0 | 23.1 | 28.7 | 98.5 | 42.0 | 75.9 | 321.2 | 39.3 |
| 24-05 | 9.1 | 195.1 | 31.9 | 18.0 | 81.9 | 32.5 | 49.3 | 318.0 | 41.2 |
| 24-11 | 7.7 | 206.5 | 27.9 | 28.4 | 91.9 | 38.5 | 68.9 | 321.6 | 39.0 |
| 28-15 | 9.0 | 220.6 | 19.3 | 26.1 | 112.6 | 43.2 | 80.0 | 327.5 | 40.9 |
| Mean | 8.1 | 204.5 | 28.1 | 25.3 | 91.2 | 37.3 | 64.2 | 320.8 | 39.6 |
| *SD* | 0.8 | 10.9 | 6.2 | 4.0 | 13.7 | 4.7 | 12.7 | 4.3 | 1.5 |
| 32-07 | 10.1 | 219.6 | 20.2 | 23.3 | 109.2 | 43.5 | 72.7 | 327.3 | 39.6 |
| 34-05 | 11.1 | 242.8 | −2.0 | 18.6 | 155.1 | 49.8 | 66.4 | 331.1 | 40.2 |
| 34-11 | 9.0 | 229.6 | 4.2 | 18.2 | 133.2 | 57.0 | 69.6 | 322.3 | 32.6 |
| 34-17 | 9.6 | 225.2 | 12.9 | 25.8 | 122.2 | 46.2 | 80.9 | 326.6 | 41.2 |
| 38-05 | 9.4 | 220.1 | 9.0 | 19.8 | 120.3 | 47.7 | 71.0 | 318.2 | 40.8 |
| 38-09 | 9.6 | 231.1 | −2.3 | 18.7 | 143.9 | 49.7 | 69.3 | 319.2 | 40.2 |
| 38-15 | 8.3 | 228.1 | 4.2 | 25.2 | 133.6 | 50.2 | 86.7 | 321.7 | 39.6 |
| Mean | 9.6 | 228.1 | 6.6 | 21.4 | 131.1 | 49.2 | 73.8 | 323.8 | 39.2 |
| *SD* | 0.9 | 7.8 | 8.1 | 3.3 | 15.4 | 4.2 | 7.3 | 3.7 | 3.0 |

*Note:* A direction indicated with a negative dip at a given azimuth is equivalent to the direction of opposite dip at the azimuth ±180°.

© 2010 The Authors, *GJI*, **181,** 303–320
Journal compilation © 2010 RAS

The Green's function $V_h(\mathbf{r}_e\,|\mathbf{r}_s)$ is straightforwardly used to combine the effects of the so-called $A$ and $B$ current electrodes and compute the electrical potential difference between the potential electrodes $M$ and $N$,

$$\Delta V(A, B, M, N) = I[V_h(\mathbf{r}_M|\mathbf{r}_A) - V_h(\mathbf{r}_M|\mathbf{r}_B) - V_h(\mathbf{r}_N|\mathbf{r}_A) + V_h(\mathbf{r}_N|\mathbf{r}_B)], \tag{5}$$

where $I$ is the electrical current actually injected during the field experiment.

### 3.2 Parametrization of the Inverse Problem

The goal of the inverse problem is to recover the conductivity tensor $\underline{\underline{\sigma}}$, that is, its six independent components. However, instead of directly looking for the $\sigma_{\alpha\beta}$ terms as in eq. (2), we reparametrize the problem in order to better account for the fact that the right quantity to be inverted is the logarithm of the conductivity. This choice is justified by the fact that the conductivity and the resistivity are reciprocal quantities, called Jeffrey's quantities by Tarantola (2006). Hence, working in the logarithmic domain makes these quantities simply opposite in sign so that formulating the inverse problem either in terms of log-conductivity or log-resistivity is indifferent. However, directly taking the logarithm of the $\sigma_{\alpha\beta}$'s may be inappropriate if the $\underline{\underline{\sigma}}$ tensor has one or more null terms. To overcome this difficulty, and following Tarantola (2006), we rewrite the conductivity tensor $\underline{\underline{\sigma}}$ as,

$$\begin{pmatrix} \sigma_{xx} & \sigma_{xy} & \sigma_{xz} \\ \sigma_{yx} & \sigma_{yy} & \sigma_{yz} \\ \sigma_{zx} & \sigma_{zy} & \sigma_{zz} \end{pmatrix} = R(\theta_x, \mathbf{x})R(\theta_y, \mathbf{y})R(\theta_z, \mathbf{z}) \begin{pmatrix} \sigma_1 & 0 & 0 \\ 0 & \sigma_2 & 0 \\ 0 & 0 & \sigma_3 \end{pmatrix}, \tag{6}$$

where $R(\theta_a, \mathbf{a})$ is a rotation matrix for angle $\theta_a$ and axis $\mathbf{a}$. Since the principal values $\{\sigma_1, \sigma_2, \sigma_3\}$ are strictly positive, taking their logarithm is always possible.

With the parametrization adopted here, a conductivity model $\mathbf{m}$ counts six parameters, $\{\log\sigma_1, \log\sigma_2, \log\sigma_3, \theta_x, \theta_y, \theta_z\}$, to be inverted. The inverse problem is non-linear and, thanks to the small number of parameters, a fully non-linear method like simulated annealing is both cheap and efficient. This method allows both to escape from local suboptimal solutions and to perform a Bayesian inversion of the data. The implementation of simulated annealing for this particular inverse problem is detailed in the Appendix.

In this study, the inversion process starts with a first model $\mathbf{m}_0$ of the Markov chain set arbitrarily at $\log\sigma_i = \log 0.1$ with $i = \{1, 2, 3\}$ and $\theta_j = 0$ with $j = \{x, y, z\}$. Then, the Metropolis algorithm turns by perturbing one parameter of the current model in the range $\mathrm{d}(\log\sigma_i) \in [-0.1; 0.1]$ or $\mathrm{d}(\theta_j) \in [-\frac{\pi}{36}; \frac{\pi}{36}]$ rad, in order to obtain a candidate model. These ranges of perturbation are chosen so that 50 per cent of the candidate models are accepted according to eq. (A1).

**Table 2.** Results of constrained inversion of each set of data of the face, without data measured in boreholes.

| Zone | $\rho_1$ (Ωm) | $Az_1$ (°N) | $\varphi_1$ (°) | $\rho_2$ (Ωm) | $Az_2$ (°N) | $\varphi_2$ (°) | $\rho_3$ (Ωm) | $Az_3$ (°N) | $\varphi_3$ (°) |
|---|---|---|---|---|---|---|---|---|---|
| 14-15 | 9.1 | 236.0 | −0.8 | 19.2 | 143.6 | 44.8 | 151.1 | 322.1 | 46.5 |
| 14-21 | 4.2 | 227.9 | −2.2 | 30.2 | 138.1 | 61.8 | 214.6 | 313.2 | 29.0 |
| 18-21 | 3.2 | 239.9 | −4.0 | 34.0 | 150.8 | 54.4 | 248.8 | 322.9 | 37.0 |
| 24-21 | 8.4 | 228.8 | 10.1 | 14.9 | 126.5 | 46.6 | 178.8 | 322.3 | 42.5 |
| 32-21 | 8.6 | 242.1 | −3.6 | 44.8 | 154.8 | 59.2 | 210.1 | 327.8 | 31.0 |
| Mean | 6.7 | 234.9 | −0.1 | 28.6 | 142.8 | 53.4 | 200.1 | 321.7 | 37.2 |
| *SD* | 2.8 | 6.4 | 5.8 | 12.0 | 11.1 | 7.5 | 37.2 | 5.3 | 7.4 |
| 16-05 | 8.7 | 189.7 | 38.4 | 29.6 | 64.4 | 36.4 | 52.6 | 308.0 | 31.1 |
| 18-09 | 7.5 | 207.7 | 27.4 | 25.9 | 89.5 | 42.2 | 60.1 | 319.1 | 35.3 |
| 20-13 | 7.4 | 207.7 | 25.3 | 31.8 | 84.9 | 49.0 | 80.7 | 313.2 | 30.0 |
| 24-05 | 8.1 | 196.8 | 29.7 | 19.4 | 82.6 | 36.0 | 44.1 | 315.2 | 39.9 |
| 24-11 | 8.3 | 214.2 | 23.9 | 33.3 | 90.4 | 51.8 | 68.7 | 317.7 | 28.0 |
| 28-15 | 10.2 | 226.0 | 14.5 | 27.9 | 116.6 | 53.5 | 89.6 | 325.0 | 33.0 |
| Mean | 8.3 | 207.0 | 26.5 | 28.0 | 88.1 | 44.8 | 66.0 | 316.4 | 32.9 |
| *SD* | 1.0 | 12.8 | 7.8 | 5.0 | 16.9 | 7.7 | 17.2 | 5.7 | 4.3 |
| 32-07 | 10.5 | 226.9 | 15.5 | 26.8 | 112 | 56.6 | 75.7 | 325.6 | 28.7 |
| 34-05 | 10.1 | 243.2 | −3.3 | 20.5 | 157.9 | 55.7 | 68.7 | 330.9 | 34.1 |
| 34-11 | 9.2 | 235.8 | −4.1 | 20.6 | 153.2 | 61.5 | 79.5 | 323.5 | 28.2 |
| 34-17 | 10.2 | 229.5 | 8.2 | 30.0 | 123.9 | 63.1 | 91.9 | 323.2 | 25.6 |
| 38-05 | 9.6 | 225.4 | 5.8 | 20.3 | 126.4 | 56.9 | 77.3 | 319.1 | 32.4 |
| 38-09 | 10.3 | 228.8 | 1.1 | 19.5 | 137.3 | 54.2 | 77.4 | 319.7 | 35.8 |
| 38-15 | 9.2 | 240.6 | −7.6 | 27.8 | 162.2 | 57.8 | 90.2 | 326.1 | 31.2 |
| Mean | 9.9 | 232.9 | 2.2 | 23.6 | 139.0 | 58.0 | 80.1 | 324.0 | 30.9 |
| *SD* | 0.5 | 7.0 | 8.1 | 4.4 | 19.2 | 3.2 | 8.2 | 4.0 | 3.6 |

*Note:* A direction indicated with a negative dip at a given azimuth is equivalent to the direction of opposite dip at the azimuth ±180°.

© 2010 The Authors, *GJI*, **181,** 303–320
Journal compilation © 2010 RAS

### 3.3 Synthetic examples

We now discuss several synthetic examples in order to illustrate some particularities of the inverse problem solved in the present study. We focus on difficulties related to the limited sampling resulting from the small number of electrode arrangements used to perform the measurements on the gallery's face. The main issue concerns the ill-posedness of the inverse problem and the non-uniqueness of its solution which is dramatically controlled by the geometry of the electrode array.

The first example shown in Fig. 7 corresponds to a situation where measurements are made with electrodes placed both on the gallery's face and in boreholes (see Fig. 5 for electrode arrangements). As can be seen in Fig. 7(a), the annealing process correctly converges towards, and the posterior probabilities (Fig. 7b) are narrow and centred on the true values given to the parameters for this synthetic example. We also performed the inversion process several times independently (in practice, we performed six independent inversions), and checked that convergence leads to very similar models statistically coherent with the true model (Fig. 7c).

The second synthetic example corresponds to a situation where measurements are limited to electrodes located on the gallery's face. This case corresponds to most measurements actually made in the underground laboratory (Fig. 4). As can be seen in Fig. 8(a), the convergence of the annealing process is obtained almost as quickly as for the preceding example, and the narrow posterior probabilities do not indicate any unresolved parameter (Fig. 8b). However, as can be observed in Fig. 8(c), the models obtained for a set of six independent inversions are scattered and may strongly depart from the true model, despite a good data-fit obtained for all the models. This indicates that the inverse problem counts many (and probably an infinite number) suboptimal solutions. This practically corresponds to the presence of unresolved parameters due to an insufficient information brought by the data. This also reveals that simulated annealing fails to discover unresolved parameters since the posterior probabilities are narrow. We interpret this failure as a consequence of the finite number of iterations performed during the final Metropolis stage: jumping from one suboptimal solution to another implies to accept transition sequences of very low probabilities models which are never accepted in practice. Consequently, the annealing remains trapped in the vicinity of a suboptimal solution. This difficulty is well known and this is why several inversion processes must be performed independently to check for the existence of a unique convergence.

The last example also corresponds to measurements made with electrodes located on the gallery's face only. However, we now complete the information brought by the data by prior information concerning the searched model. In practice, this is done by generating the Markov chain of models in a limited domain: the parameters $\rho_i$ are searched in the range $\rho_{i\text{true}} \pm 25$ per cent with $i = \{1, 2, 3\}$, and the parameters $\theta_j$ are searched in the range $\theta_{j\,\text{true}} \pm \frac{\pi}{9}$ rad with $j = \{x, y, z\}$. Again, the annealing process correctly converges (Figs 9a and b), and one can observe that the models obtained for 6 independent inversions are clustered around the true model (Fig. 9c), with standard deviations significantly lower than the size of the authorized domain. Fig. 10 illustrates how the azimuths and dips vary when the parameters $\theta$ span the whole range $\theta_{\text{true}} \pm \frac{\pi}{9}$ rad. This last synthetic example shows that the lack of data obtained in boreholes can be compensated by reasonable prior information that dramatically reduces the non-uniqueness of the inversion.

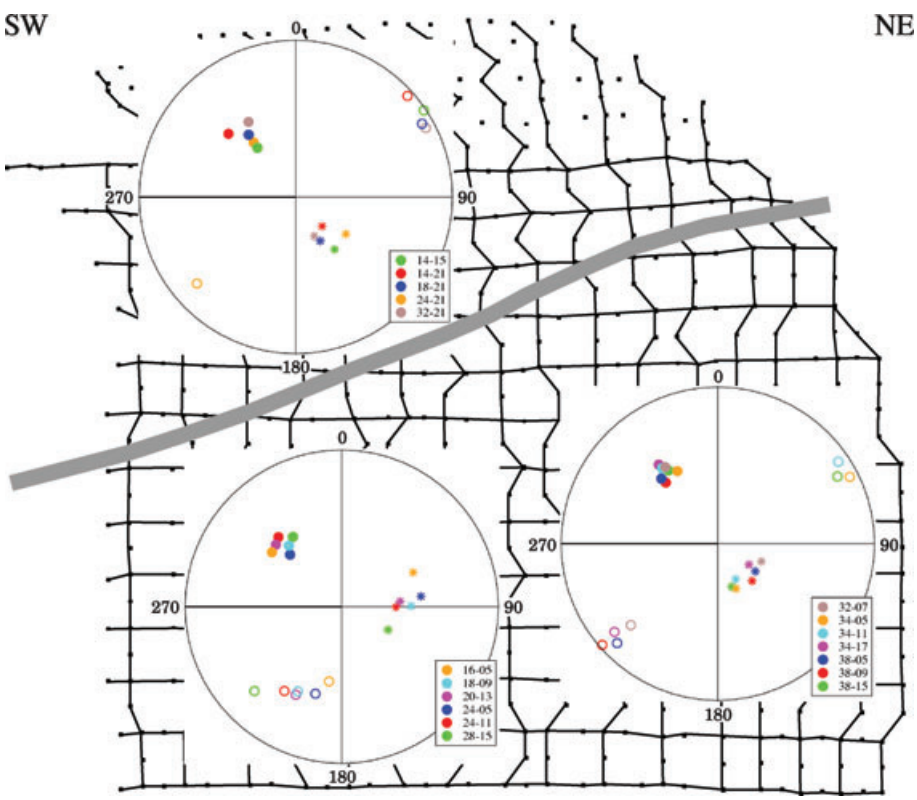


**Figure 11.** Wulff stereographic projection (angle preserving, lower hemisphere) showing the results of constrained inversion of each set of data of the face, without data measured in boreholes. The maximum value of resistivity is plotted with a filled circle, the minimum value of resistivity is plotted with an empty circle, and the intermediate value of resistivity is plotted with a star.

© 2010 The Authors, *GJI*, **181,** 303–320
Journal compilation © 2010 RAS

The three synthetic examples discussed in this section show that simulated annealing efficiently converges towards the true model provided either borehole data are available or prior information can be used. Inverting surface data alone conducts to convergence towards suboptimal models, which may strongly depart from the true model.

## 4 INVERSION OF THE DATA

The 18 data sets measured on the Ga04 face were inverted independently, using the two processes described above: inversion using borehole data and inversion using prior information, more simply called constrained inversion. For the unconstrained inversion, data measured in the group of boreholes located above the main fracture were used with each of the five data sets located in the upper domain of the face, while data measured in the group of boreholes located below the main fracture were used with each of the 13 data sets located in the lower domain of the face. Then, the model found by this first process is used as prior information for the constrained inversion performed with limited ranges of perturbations ($\rho \pm 25$ per cent and $\theta \pm \frac{\pi}{9}$ rad). At the end of the inversion, the parameters $\{\theta_x, \theta_y, \theta_z\}$ of the model are converted into principal directions $\{Az_1, \varphi_1; Az_2, \varphi_2; Az_3, \varphi_3\}$ of the resistivity tensor, where $Az$ and $\varphi$ are the azimuth and the dip, respectively. The values found by inversion using borehole data are given in Table 1, and the values found by constrained inversion are given in Table 2. Mean and standard deviation are computed from results belonging to three zones: the upper domain located above the main fracture (five data sets), the SW half of the lower domain (six data sets), and the NE half of the lower domain (seven data sets). All these results do not present significant differences between unconstrained inversion and constrained inversion: for the resistivity, the differences are much lower than $\pm 25$ per cent, and for the azimuth and dip, the differences are much lower than the ones corresponding to variations of $\pm\frac{\pi}{9}$ authorized for the parameters $\theta$. So, we discuss further only the results of the constrained inversion.

The directions of the principal values of the resistivity tensor found by constrained inversion of each of the 18 data sets are presented in Fig. 11. The three zones defined in Table 2 are plotted in three diagrams showing the Wulff stereographic projection (angle preserving, lower hemisphere). First, whatever the zone, the direction of maximum resistivity is very concentrate ($Az = 321.7°$ N $\pm$ $5.3°$, $\varphi = 37.2° \pm 7.4°$ for the upper zone, $Az = 316.4°$ N $\pm$ $5.7°$, $\varphi = 32.9° \pm 4.3°$ for the SW half of the lower domain, and $Az = 324°$ N $\pm 4°$, $\varphi = 30.9° \pm 3.6°$ for the NE half of the lower domain). On the other hand, the intermediate and lower values of resistivity are more scattered, especially in the lower domain. Fig. 12 shows the orientations of the normals to the medium planes defined by 32 electrodes in each of the 18 areas. This plot clearly shows the curved shape of the face, with a rotation of the azimuth particularly visible on the SW side (stars and empty circles). In the diagram of the SW lower domain in Fig. 11, the directions of intermediate and minimum values of resistivity spread according to the variation of the azimuth of the normal to the face shown in Fig. 12, except the ones of the area called 24-05. For the five other areas of this zone, the angle between the direction of the minimum resistivity and the normal to the face equals $90.4° \pm 2.6°$, and if we consider the 18 areas, this angle equals $87° \pm 16.2°$. This result shows that the direction of minimum resistivity is always contained in the medium local plane of the face.

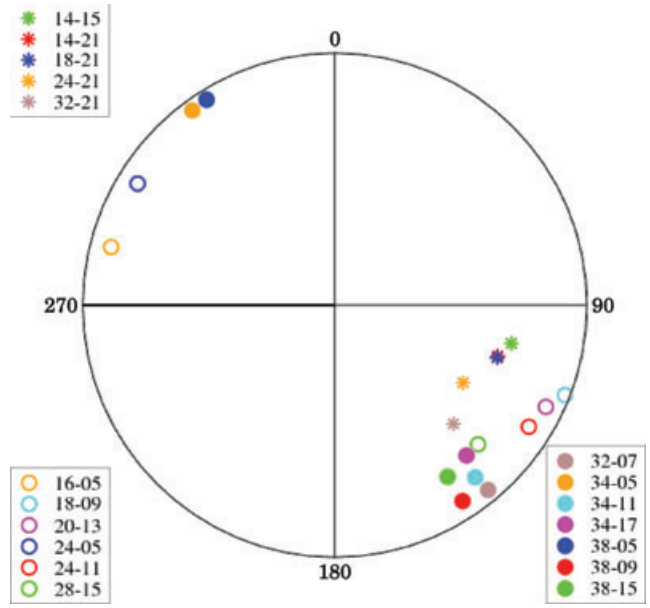


**Figure 12.** Wulff stereographic projection (angle preserving, lower hemisphere) showing the orientations of the normals to the medium planes, each defined by a group of 32 electrodes used for anisotropy measurements.

## 5 DISCUSSION

The directions of the principal values of the resistivity tensor obtained from the inversions discussed in the preceding sections are plotted in Fig. 13. One can observe that the direction of maximum resistivity is almost constant and departs of less than 10° from the direction normal to the bedding plane. This difference is not

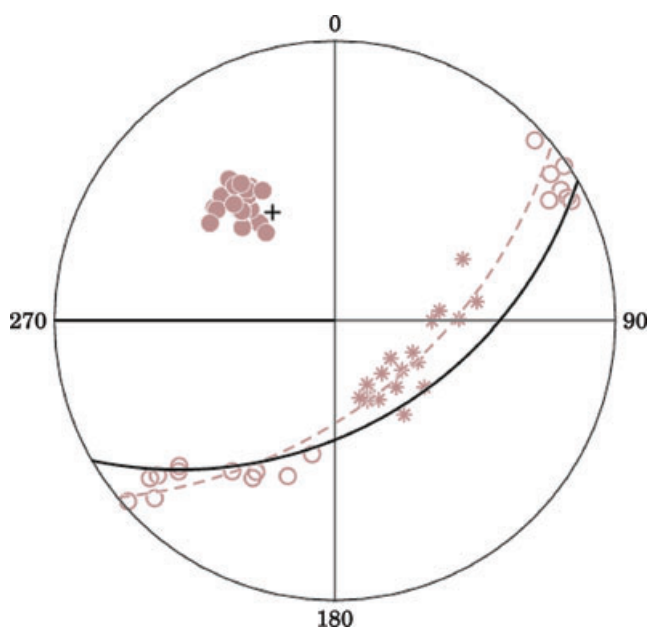


**Figure 13.** Wulff stereographic projection (lower hemisphere) showing all the results of constrained inversion of the sets of data of the face. The maximum value of resistivity is plotted with a filled circle, the minimum value of resistivity is plotted with an empty circle, and the intermediate value of resistivity is plotted with a star. The plane N 51–57°, normal to the direction of the mean value of maximum resistivity, is represented with a dashed line. The bedding plane (N 60–48°) is represented with a black line and its normal with a black cross.

© 2010 The Authors, *GJI*, **181,** 303–320
Journal compilation © 2010 RAS

significant when considering the variability of the bedding direction observed across the gallery's face. Consequently, the other two directions of the intermediate resistivity and minimum resistivity are contained in the bedding plane. The direction of minimum resistivity is contained in the face plane as shown previously and the intermediate resistivity component is perpendicular to the face.

The geometrical characteristics of the resistivity tensor appear controlled by both the stratigraphic directions and the geometry of the gallery which, in turn, determines the spatial organization of the stress perturbations in the rock mass. Owing to both the mineralogical structure and the stratigraphic characteristics of Opalinus clay, the resistivity tensor should be approximately transversely isotropic with respect to the normal to the bedding plane. The deviation from transverse isotropy may be explained by the superimposition of a secondary anisotropy produced by the combination of both others fault systems which are not parallel to the bedding planes (e.g. SW-dipping faults and Rhenish NNE trending faults) and the presence of EDZ unloading microfractures oriented parallel to the gallery face. The existence of these microfractures may be due to both stress redistribution and desaturation.

Concerning the values of resistivity found by inversion, Table 2 shows that the minimum and intermediate values do not vary significantly from one area to the other ($\rho_1 = 8.5\,\Omega\text{m} \pm 2\,\Omega\text{m}$ and $\rho_2 = 26.5\,\Omega\ \text{m} \pm 7.3\,\Omega\ \text{m}$) while the maximum value is very different between the two domains separated by the main fracture ($\rho_3 = 200.1\,\Omega\ \text{m} \pm 37.2\,\Omega\ \text{m}$ in the upper domain and $\rho_3 = 73.6\,\Omega\ \text{m} \pm 14.5\,\Omega\ \text{m}$ in the lower domain). The maximum values of resistivity are displayed in Fig. 14, located on the Ga04 face at the place of the 18 areas of measurement. The main fracture visible on the face clearly separates two domains: an upper domain characterized by high resistivity values and a lower domain characterized by low resistivity values. These results confirm the paradox of anisotropy present in measurements made with aligned electrodes since Fig. 3 shows the exactly opposite image.

The vertical cross-section on Fig. 15 shows that the investigated area, called EZ-G section, is mainly characterized by tectonic fractures subparallel to the bedding planes and dipping to SE with an angle of about 45°. In this section, two faults seem to have played a significant role (thicker line). These faults suggest that slip occurred between the bedding planes during the Jura folding of the Mont Terri anticline. A significant low angle SW-dipping fault outcrops on the Ga04 face. This major fault extends through the Gallery Ga04 along more than 40 m and disappears into the ceiling (not visible on Fig. 15). Since these both faults systems dip with different orientations, the resulting structural pattern of the EZ-G section is very heterogeneous. Two resin injections have been performed in order to impregnate the fracture network behind the Ga04 face before the excavation of the EZ-G section. Resin flow paths drawn on Fig. 15 indicate that pre-existing tectonic fault fractures acted as preferential flow paths. In fact, the EDZ fracture network developed behind the Ga04 face is mainly made of reactivated pre-existing SE- and SW-dipping tectonic faults. New true EDZ fractures are scarce in the investigated area; they are oriented parallel to the Ga04 face and may be identified only at microscale scale.

Since the Ga04 face was exposed to tunnel ambient air during about four years and was not covered by a shotcrete layer,

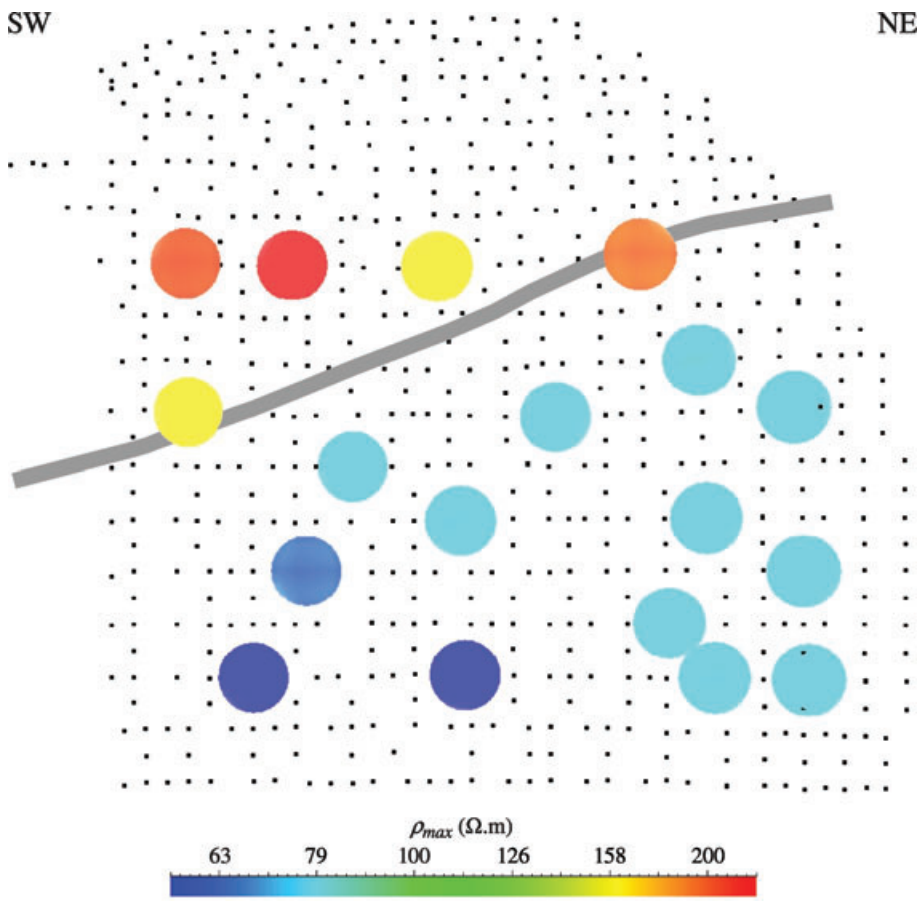


**Figure 14.** Maximum value of the resistivity tensor found by constrained inversion in the 18 areas of the face.

© 2010 The Authors, *GJI*, **181,** 303–320
Journal compilation © 2010 RAS

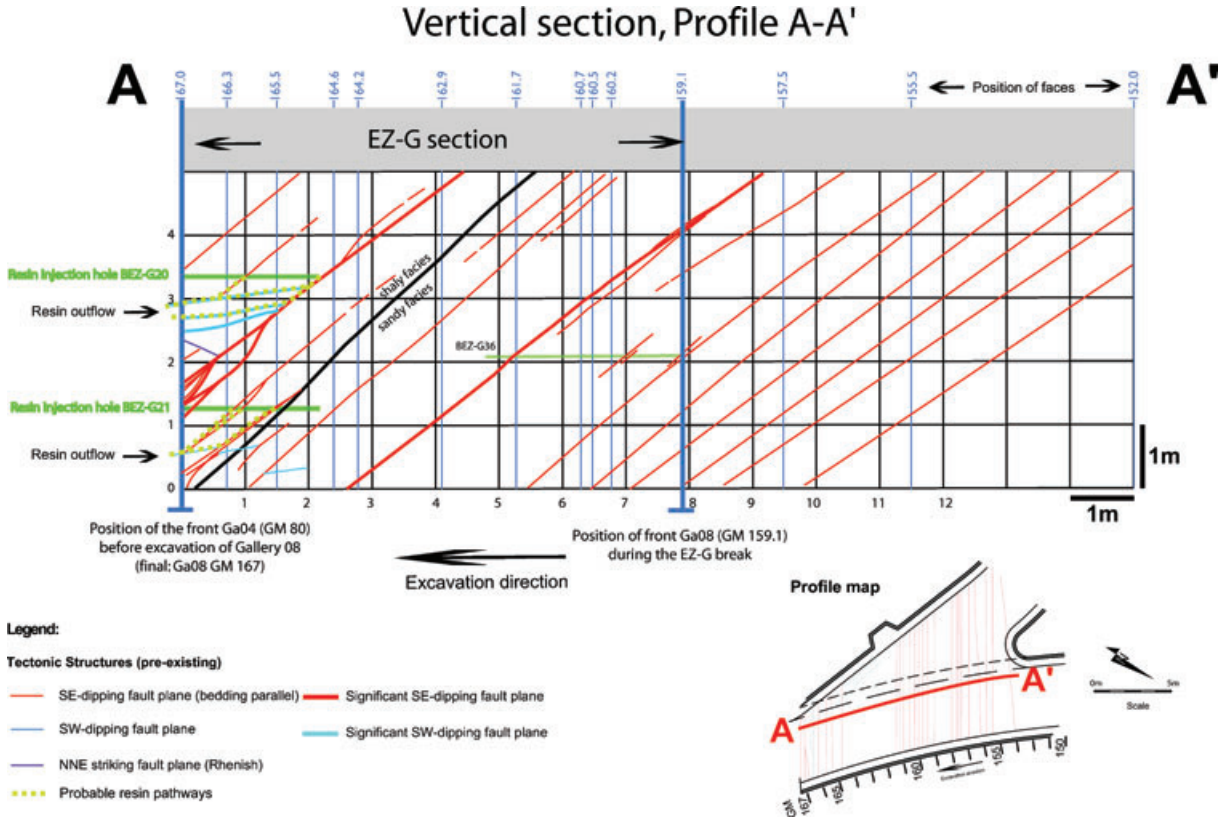


**Figure 15.** Global view of the tectonic and geological structures in the studied EZ-G section recognized during the excavation of the gallery Ga08.

significant desaturation could occurred along these fractures and especially along the bedding planes. The desaturation of bedding planes produced a reduced electrical contact between adjacent planes. This may explain the higher resistivity values measured above the major SE-dipping fault intersecting the Ga04 face (Fig. 15). By contrast, wet spots and water outflows from three boreholes drilled in the lower compartment of this major fault have been observed. This humidity has certainly contributed to avoid any desaturation of this rock mass part and hence maintaining the electrical contact between the beds and the faults.

## 6 CONCLUSION

The present study shows that the anisotropy of electrical resistivity observed at the scale of several metres results from complex interactions between inherited tectonic features, stratigraphic properties and stress perturbations produced by the excavation of the gallery. The behaviour of rock-mass domains depends on their location relative to the tectonic structures in combination with their intrinsic characteristics (i.e. bedding direction).

From a methodological point of view, it must be noticed that the important anisotropy of electrical resistivity observed in the EZ-G section appeals for sophisticated 3-D inversion methods able to tackle with anisotropy. As demonstrated by Greenleaf *et al.* (2003), an isotropic conductivity distribution can be found that reproduces the data acquired on anisotropic media. It is then particularly hazardous to invert such data with a method that assumes an isotropic conductivity, and strong bias may occur. For instance, inverting the data shown in Fig. 3 with an isotropic approach would inevitably produce resistivity sections affected by the same paradox as present in the pseudo-sections of apparent resistivity. However, while presenting approximate and qualitative pseudo-sections immediately warns the reader against possible artefacts (including the anisotropy paradox), producing inverted resistivity sections could be misleading because of their assumed quantitative appearance. So, in such a case, we recommend not using inappropriate isotropic inverse methods.

## ACKNOWLEDGMENTS

This work benefited of the invaluable support from FORPRO colleagues Michel Cathelineau, Joël Lancelot, Annie Le Bauzec, Patrick Pinettes, and Patrick Verdoux, ANDRA colleagues, Jacques Delay and Patrick Lebon, and Paul Bossart from Swisstopo. The field experiments have been greatly improved by the assistance of Thierry Theurillat, Claude Girardin, Gilbert Jolliat and Vincent Risse, from the Mont Terri staff, and Bruno Kergosien from CNRS. This work is financially supported by the CNRS and ANDRA through the GNR FORPRO II and corresponds to the GNR ForPro II contribution number 2009-1. This paper is also IPGP contribution number 2530. Great thanks to the editor, Dr. Mark Everett, and to an anonymous reviewer for their constructive remarks that allowed us to improve our manuscript.

## REFERENCES

Apparao, A., Rao, T.G., Sastry, R.S. & Sarma, V.S., 1992. Depth of detection of buried conductive targets with different electrode arrays in resistivity prospecting, *Geophys. Prospect.,* **40,** 749–760.

Barker, R.D., 1989. Depth of investigation of collinear symmetrical four-electrodes arrays, *Geophys.,* **54,** 1031–1037.

Bhanot, G., 1988. The metropolis algorithm, *Rep. Prog. Phys.,* **51,** 429–457.

Blümling, P., Bernier, F., Lebon, P. & Martin, C.D., 2007. The excavation damaged zone in clay formations time-dependent behaviour and influence on performance assessment, *Phys. Chem. Earth,* **32,** 588–599, doi:10.1016/j.pce.2006.04.034.

Bossart, P., Meier, P., Moeri, A., Trick, T. & Mayor, J.-C., 2002. Geological and hydraulic characterisation of the excavation disturbed zone in the Opalinus Clay of the Mont Terri Rock Laboratory, *Eng. Geol.,* **66,** 19–38.

Bossart, P., Trick, T., Meier, P. & Mayor, J.-C., 2004. Structural and hydrogeological characterisation of the excavation-disturbed zone in the Opalinus Clay (Mont Terri Project, Switzerland), *Appl. Clay Sci.,* **26,** 429–448.

Bossart, P. & Thury, M. (eds), 2008. Mont Terri Rock Laboratory Project, Programme 1996 to 2007 and Results, Rep. Swiss Geological Survey 3, Wabern, Switzerland.

Das, U.C. & Li, P., 1996. Analytical solution for direct current electrical potentials in an arbitrarily anisotropic half-space, *J. Appl. Geophys.,* **35,** 63–67.

Edwards, L.S., 1977. A modified pseudo-section for resistivity and induced polarization, *Geophysics,* **42,** 1020–1036.

Gibert, D., Nicollin, F., Kergosien, B., Bossart, P., Nussbaum, Ch., Grislin-Mouëzy, A., Conil, F. & Hoteit, N., 2006. Electrical tomography monitoring of the excavation damaged zone of the Gallery 04 in the Mont Terri rock laboratory: field experiments, modelling, and relationship with structural geology, *Appl. Clay Sci.,* **33,** 21–34, doi:10.1016/j.clay.2006.03.008.

Greenleaf, A., Lassas, M. & Uhlmann, G., 2003. Anisotropic conductivities that cannot be detected by EIT, *Physiol. Meas.,* **24,** 413–419.

Habberjam, G.M., 1972. The effects of anisotropy on square array resistivity measurements, *Geophys. Prospect.,* **20,** 249–266.

Hunsche, U., Walter, F. & Schnier, H., 2004. Evolution and failure of the Opalinus clay: relationship between deformation and damage, experimental results and constitutive equation, *Appl. Clay Sci.,* **26,** 403–411.

Kruschwitz, K. & Yaramanci, U., 2004. Detection and characterisation of the disturbed rock zone in claystone with the complex resistivity method, *J. appl. Geophys.,* **57,** 63–79.

Li, P. & Uren, N.F., 1997. The modelling of direct current electric potential in an arbitrarily anisotropic half-space containing a conductive 3-D body, *J. appl. Geophys.,* **38,** 57–76.

Martin, D., Lanyon, G.W., Bossart, P. & Blümling, P., 2004. Excavation Disturbed Zone (EDZ) in Clay Shale: Mont Terri, Mont Terri Publications, TN 2001-01.

McEwen, T., (ed.), 2002. Characterisation and representation of the excavation disturbed or damaged zone (EDZ), Organisation for Economic Co-operation and Development, report NEA/RWM(2002)1, 83 pp.

Meier, P., Trick, Th., Blümling, P. & Volckaert, G., 2000. Self-healing of fractures within the EDZ at the Mont Terri Rock Laboratory: results after one year of experimental work, in *Proceedings of International Workshop on Geomechanics, Hydromechanical and Thermohydro-mechanical Behaviour of Deep Argillaceous Rocks: Theory and Experiment,* October 11–12th, 2000, Paris.

Metropolis, N., Rosenbluth, A., Rosenbluth, N., Teller, A. & Teller, E., 1953. Equation of the state calculations by fast computing machines, *J. Chem. Phys.,* **21,** 1087–1092.

Nicollin, F., Gibert, D., Bossart, P., Nussbaum, Ch. & Guervilly, C., 2008. Seismic tomography of the Excavation Damaged Zone of the Gallery 04 in the Mont Terri Rock Laboratory, *Geophys. J. Int.,* **172,** 226–239, doi:10.1111/j.1365-246X.2007.03615.x

Schuster, K., Alheid, H.-J. & Böddener, D., 2001. Seismic investigation of the excavation damaged zone in Opalinus Clay, *Eng. Geol.,* **61,** 189–197.

Senos Matias, M.J., 2002. Square array anisotropy measurements and resistivity sounding interpretation, *J. appl. Geophys.,* **49,** 185–194.

Tarantola, A., 2006. *Elements for Physics: Quantities, Qualities and Intrinsic Theories*. Springer, Berlin, 263 pp.

Thury, M. & Bossart, P., 1999. The Mont Terri rock laboratory, a new international research project in a Mesozoic shale formation, in Switzerland, *Eng. Geol.,* **52,** 347–359.

## APPENDIX A: IMPLEMENTATION OF SIMULATED ANNEALING

The simulated annealing is based on the Metropolis algorithm which is a Markov Monte Carlo Chain generating a series of models $\{\mathbf{m}_0, \mathbf{m}_1, \mathbf{m}_2, \cdots, \mathbf{m}_k, \cdots\}$ such that their statistical distribution satisfies an arbitrary probability density fonction $\varrho(\mathbf{m})$ (Metropolis *et al.* 1953; Bhanot 1988). The Metropolis sequence is constructed on an accept/reject rule which reads,

$$\text{prob}[\mathbf{m}_{k+1} = \mathbf{m}_{\text{try}}] = \min\left[1, \frac{\varrho(\mathbf{m}_{\text{try}})}{\varrho(\mathbf{m}_k)}\right], \tag{A1}$$

where $\mathbf{m}_k$ is the last model included in the sequence and $\mathbf{m}_{\text{try}}$ is a candidate model which may eventually be included in the sequence. The Metropolis rule is such that a candidate model with a higher probability [i.e. $\varrho(\mathbf{m}_{\text{try}}) \geq \varrho(\mathbf{m}_k)$] is always incorporated in the sequence while a less-probable model [i.e. $\varrho(\mathbf{m}_{\text{try}}) < \varrho(\mathbf{m}_k)$] is only sometimes accepted. When the random assignment given by eq. (A1) fails and $\mathbf{m}_{\text{try}}$ is rejected, the replication rule $\mathbf{m}_{k+1} = \mathbf{m}_k$ is used.

Simulated annealing consists in running the Metropolis algorithm while progressively morphing the probability density $\varrho(\mathbf{m})$ from the uniform distribution to the desired probability $\varrho_1(\mathbf{m})$. This is practically done through the use of a control parameter $T$, called the temperature, such that,

$$\varrho_T(\mathbf{m}) = K_T \exp\left[\frac{\log \varrho_1(\mathbf{m})}{T}\right], \tag{A2}$$

where $K_T$ is a normalizing constant. One can verify that $\varrho_\infty(\mathbf{m})$ is a constant $K_\infty$. If the probability density possesses an absolute maximum at $\mathbf{m}_{\text{best}}$, then $\varrho_0(\mathbf{m}) = \delta(\mathbf{m} - \mathbf{m}_{\text{best}})$ with $\delta$ the Dirac distribution.

By running the Metropolis algorithm while decreasing the temperature from infinity to zero, the sequence of accepted models is progressively guided towards the regions of the models space where the probability is maximum. This guidance is achieved by giving some memory to the Markov chain, that is, by imposing a strong correlation among neighbouring models in the sequence. This is practically done by constructing the candidate model, $\mathbf{m}_{\text{try}}$, via perturbing one randomly chosen parameter of the current model $\mathbf{m}_k$.

In the Bayesian approach, the probability generally reads $\varrho_1(\mathbf{m}) = P(\mathbf{m})\, L(\mathbf{d}|\mathbf{m})$ where $P$ and $L$ are the prior and likelihood probabilities, respectively, and $\mathbf{d}$ is the data set. In the present study the prior probability is not considered since the whole space model is allowed to be explored by simulated annealing, and $\varrho_1(\mathbf{m}) = L(\mathbf{d}|\mathbf{m})$.

When starting the inversion of a given data set, the likelihood $L(\mathbf{d}|\mathbf{m})$ is approximately known and a two-step inversion is necessary to perform a Bayesian analysis. First, a simulated annealing optimization is performed to converge towards a model with a high (hopefully the highest) probability. During this stage, $L(\mathbf{d}|\mathbf{m})$ is not precisely determined and a proxy is used instead (e.g. a generic multivariate Cauchy distribution). Once a high-probability model is obtained, a statistical analysis of the residuals (i.e. $\mathbf{d} - \mathbf{d}_{\text{m}}$ where $\mathbf{d}_{\text{m}}$ is the synthetic data vector produced by the high-probability

model **m**) is performed to both check the validity of the proxy probability and to determine its parameters (e.g. mean, variance, etc.) to obtain $\varrho_1(\mathbf{m})$. The second stage of the inversion may then be performed by running the Metropolis algorithm in order to obtain a series of models distributed according to the probability $\varrho_1(\mathbf{m})$. A statistical analysis of this series of models allows to derive the posterior Bayesian marginal probabilities for the model parameters of interest.

© 2010 The Authors, *GJI*, **181,** 303–320
Journal compilation © 2010 RAS